Supporting Information

Jariwala et al. 10.1073/pnas.1317226110

SI Text

Materials and Device Fabrication. *Raman spectroscopy of MoS_2.* The monolayer character of the MoS_2 flake samples was confirmed via Raman spectroscopy. The Raman spectra were acquired using a 532-nm laser with a 100× objective (NA = 0.9) in a scanning confocal microscope (WITec Alpha300 R). The separation between E_{2g} and A_{1g} modes of MoS_2 (Δ) is a well-known parameter for identifying layer thickness in ultrathin MoS_2 flakes. Typically, a Δ value of <20 cm^{-1} indicates a single layer sample (1). Fig. S1 shows the Raman spectrum ($\Delta\sim$ 17.7 cm^{-1}) of a representative flake that was fabricated into a p-n heterojunction device.

Sorting and deposition of semiconducting single-walled carbon nanotubes. Semiconducting single-walled carbon nanotubes (SWCNTs) with ∼99% semiconductor purity were isolated by density gradient ultracentrifugation following the procedure discussed in a previous report (2). SWCNT thin films were prepared by vacuum filtration and transferred onto prepatterned Au electrodes by the acetone bath transfer method as outlined in the literature (2, 3). The semiconducting purity of the sorted SWCNTs was estimated using the optical absorbance characterization and an analysis protocol developed earlier (3, 4). Fig. S2 shows the optical absorbance spectra for as-purchased arc-discharge SWCNTs (P2; Carbon Solutions) and sorted ∼99% semiconductor purity SWCNTs. The average diameter of the semiconducting tubes is 1.4 nm.

All devices were fabricated on 300-nm-thick SiO_2/Si substrates. The Si <100> wafers were purchased from Silicon Quest International. The wafers were doped n-type with As (resistivity = 0.001–0.005 Ω-cm). The MoS_2 field-effect transistors (FETs) were fabricated using previously reported techniques (5). Specifically, bulk MoS_2 crystals were purchased from SPI Supplies and mechanically exfoliated using clear adhesive tape. The flakes were identified using an optical microscope (Olympus BX 51M) and then subjected to electron beam lithography (EBL). A two-step EBL process was adopted to fabricate Au contacts with no adhesion layer. The patterns in the first step were designed to be just short of touching the MoS_2 flakes. Au (75 nm thick) is the metal in contact with the MoS_2 flake. Following liftoff in acetone, the devices were further cleaned with remover PG (Microchem) at 60 °C for 1 h.

A portion of the MoS_2 FET including both the contacts and channel was exposed in a subsequent step of EBL. Atomic layer deposition (ALD; Cambridge Nanotech, Savannah S100) was used to grow 30-nm alumina at 100 °C to insulate the MoS_2 channel and contacts, thus prevent shorting following subsequent SWCNT deposition. Trimethyl aluminum (TMA) (Aldrich, 99%) was used as the precursor for ALD growth of alumina, and ultrahigh purity nitrogen (Airgas) was used as the purging gas. A single ALD cycle consisted of a TMA pulse for 0.015 s and a 30-s purge, followed by a H_2O pulse for 0.015 s and a second 30-s purge. The growth rate was determined to be ∼0.75 Å/cycle. A total of 400 cycles was performed to achieve 30 nm thickness. The oxide was lifted off in warm acetone at 50 °C for 1 h. A cellulose membrane containing the semiconducting SWCNT film was then stamped onto the entire substrate and dissolved under acetone vapor as outlined in previous reports (2). The SWCNT film was annealed in vacuum (50 mTorr) at 200 °C for 1 h and then patterned with EBL using a ZEP 150 (Nippon Zeon) resist. Reactive ion etching (Samco RIE-10 NR) in an oxygen plasma atmosphere (100 mW, 15 s, 20 sccm) was then used to etch the nanotubes. The resist was subsequently dissolved in hot (80 °C) *N*-methyl-2- pyrrolidone for ∼6 h. The SWCNT film morphology close to the junction region was characterized using AFM as shown in Fig. S3.

Electrical and Photocurrent Measurements. Output and transfer characteristics were measured using Keithley 2400 source meters and custom LabView programs. The gate voltage was swept at 10 V/s in steps of 1 V in the transfer and output plots shown in Fig. 2*B*.

The p-n heterojunction diode was used as a half-wave rectifier using the circuit outlined in the inset of Fig. 2*D*. A 1-MΩ resistor was used in series with the device to limit the current. A sinusoidal wave from a waveform generator was used as the input, whereas the output current was measured using a preamplifier (1211 DL Instruments) and the output voltage as it would appear across a 1-MΩ resistor (schematic in Fig. 2*D*). Time domain waveforms were captured using an oscilloscope.

A scanning confocal microscope (100× objective with NA = 0.9; WiTec system) coupled to a tunable coherent white light source (NKT Photonics) was used to generate the spatially resolved photocurrent, which was converted into a voltage by a current preamplifier and recorded by either a lock-in amplifier (for imaging) or a digital sampling oscilloscope (for temporally resolved measurements). The junction area was subjected to global illumination using the same apparatus with a 20× objective. The current-voltage (*I-V*) characteristics under global illumination were acquired using the same Keithley 2400 source meters and custom LabView programs.

Analysis of Current Voltage Characteristics. *Junction transfer characteristics, contact resistance, and sheet resistance.* Linear and semi-log transfer characteristics of the junction are shown in Fig. S4. The channel resistances of the individual MoS_2 and CNT FETs were estimated at $V_G = 0$ V by subtracting the contact resistance values reported in literature from the $(dI/dV)^{-1}$ values obtained using the *I-V* plots shown in Fig. S5. The channel resistance of the CNT FET at $V_G = 0$ V is estimated to be ∼0.66 MΩ, whereas that of the MoS_2 FET is ∼0.39 MΩ. These channel resistance values are >15 times smaller than the junction resistance $[(dI/dV)^{-1}$ near $V_D = 0$ V] of ∼11.6 MΩ obtained from Fig. 2*A*. Assuming that the length of the nonjunction portions of single layer (SL)-MoS_2 and s-SWCNT film are the same as their respective FET channels, the resistance of the junction after subtracting the series resistances of the nonjunction portions and the contact resistances is about 10.4 MΩ. Thus, the junction resistance dominates even in presence of series resistances at $V_G = 0$. However, this situation changes under depletion gate biases of either the s-SWCNTs or MoS_2, which leads to the antiambipolar behavior with two off states at either extremes in gate voltage.

Data fitting to the Shockley equation. The diode output curves with varying gate bias (V_G) were fit with the Shockley diode equation, $|I_D| = |I_{rs}|\left(e^{\frac{eV_D}{nk_BT}} - 1\right)$, where I_D is the drain current, V_D is the drain bias, I_{rs} is the reverse saturation current at $V_D = -0.05$ V, e is the electronic charge, n is the ideality factor, k_B is the Boltzmann constant, and T is the temperature of operation (300 K). The best fit to the diode curve ($r^2 > 99\%$) is achieved for V_G values ranging from −30 to −60 V, with the diode ideality factor (n) approaching closest to 1 at −40 V (Fig. S6). The *I-V* curves at other gate biases fit poorly to the Shockley equation ($r^2 < 70\%$).

Spatial Mapping of Photoluminescence and Raman Shift. Spatial Raman and photoluminescence (PL) mapping was performed on

the heterojunction device. A spatial map of the Raman 2G peak (3,100–3,250 cm^{-1}) from the SWCNTs and photoluminescence from the SL-MoS_2 at 3,700–3,900 cm^{-1} (A peak) shows that the photocurrent arises only from the junction region. It was also observed that that the PL signal was uniform in the junction area of the MoS_2 flake compared with the protected/masked area as seen in Fig. S7.

Power dependence of photocurrent. The power dependence of the photocurrent was measured under zero bias using the same illumination system (Fig. S8). The power dependence is sublinear, which is consistent with bimolecular recombination of electrons and holes, further implying that the concentration of photogenerated carriers is similar to or greater than the intrinsic carrier concentration (6).

Calculation of responsivity and quantum efficiency. The quantum efficiency was calculated using the formula $EQE = \frac{I_{ph}/e}{P/h\nu} \times 100$, where I_{ph}, e, P, and $h\nu$ represent the photocurrent, electronic charge, incident optical power, and photon energy, respectively. The photocurrent was extracted by subtracting the dark I-V curves from the illuminated I-V curves. The responsivity (R) was calculated using $R = EQE \times 1.24/\lambda$, where λ is in micrometers.

1. Lee C, et al. (2010) Anomalous lattice vibrations of single- and few-layer MoS_2. *ACS Nano* 4(5):2695–2700.
2. Sangwan VK, et al. (2012) Fundamental performance limits of carbon nanotube thin-film transistors achieved using hybrid molecular dielectrics. *ACS Nano* 6(8):7480–7488.
3. Green AA, Hersam MC (2011) Nearly single-chirality single-walled carbon nanotubes produced via orthogonal iterative density gradient ultracentrifugation. *Adv Mater* 23(19):2185–2190.
4. Arnold MS, Green AA, Hulvat JF, Stupp SI, Hersam MC (2006) Sorting carbon nanotubes by electronic structure using density differentiation. *Nat Nanotechnol* 1(1):60–65.
5. Jariwala D, et al. (2013) Band-like transport in high mobility unencapsulated single-layer MoS_2 transistors. *Appl Phys Lett* 102(17):173107.
6. Bube RH (1992) *Photoelectronic Properties of Semiconductors* (Cambridge Univ Press, Cambridge, UK).

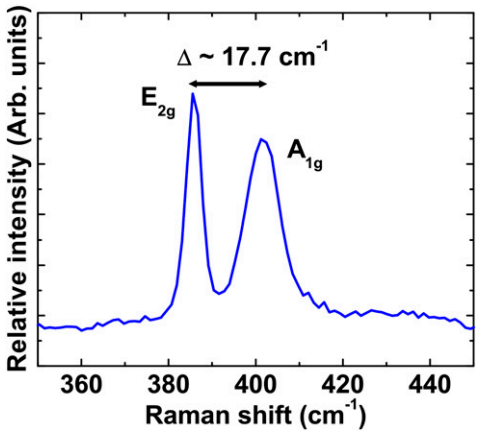

Fig. S1. Raman spectrum of a representative MoS_2 flake. The separation of 17.7 cm^{-1} between the E_{2g} and A_{1g} features indicates monolayer thickness.

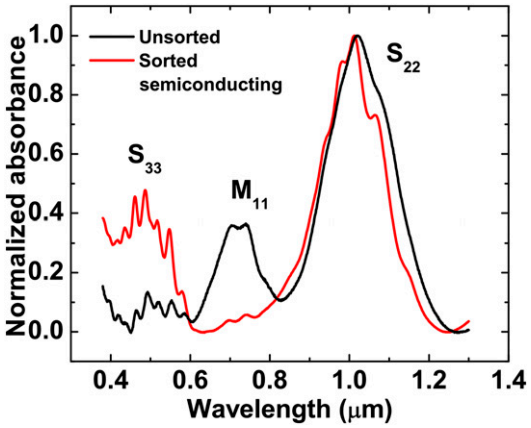

Fig. S2. Normalized optical absorbance spectra of arc discharge SWCNTs. The unsorted SWCNTs (black) consist of a mixture of metallic and semiconducting species as evidenced by the presence of both semiconducting (S_{22} and S_{33}) and metallic (M_{11}) peaks, whereas the spectrum of the sorted semiconducting SWCNTs (red) shows strong semiconducting peaks and negligible metallic peaks.

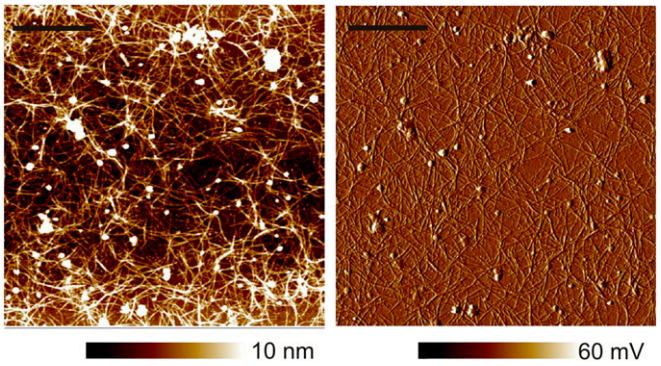

Fig. S3. Atomic force microscopy (AFM) images of the SWCNT film. Topographic image (*Left*) and amplitude error (*Right*) show the random network morphology and uniform coverage of SWCNTs. (Scale bar, 1.5 μm.)

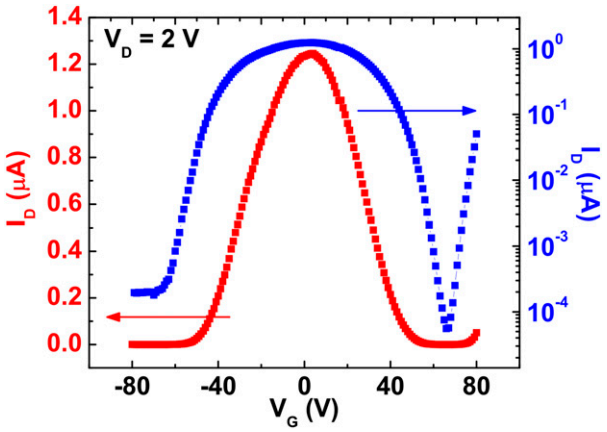

Fig. S4. Linear (red) and semilog (blue) transfer characteristics of a representative p-n heterojunction diode showing antiambipolar behavior and on/off ratio exceeding 10^4.

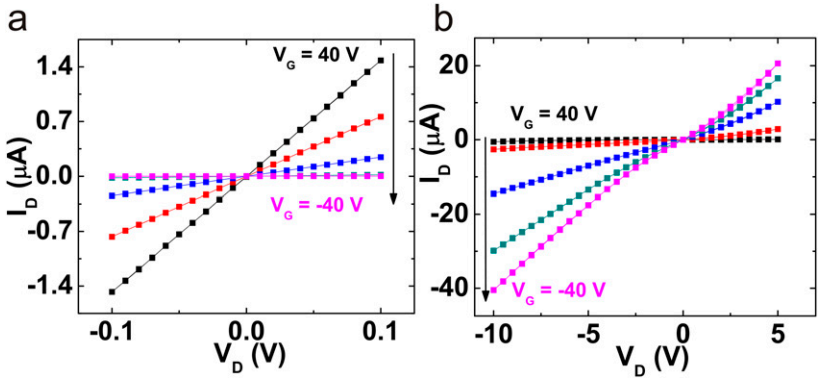

Fig. S5. (*A*) Output plots of a representative SL-MoS_2 FET showing linear *I-V* characteristics and n-type behavior. (*B*) Output plots of a representative s-SWCNT FET showing p-type behavior.

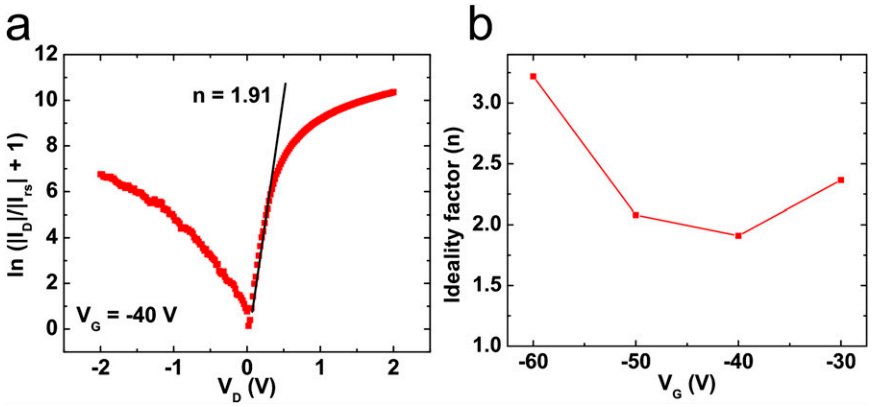

Fig. S6. (*A*) Shockley diode equation fit to the output curve at $V_G = -40$ V. (*B*) Variation of n with V_G shows that the diode is closest to ideal behavior at $V_G = -40$ V.

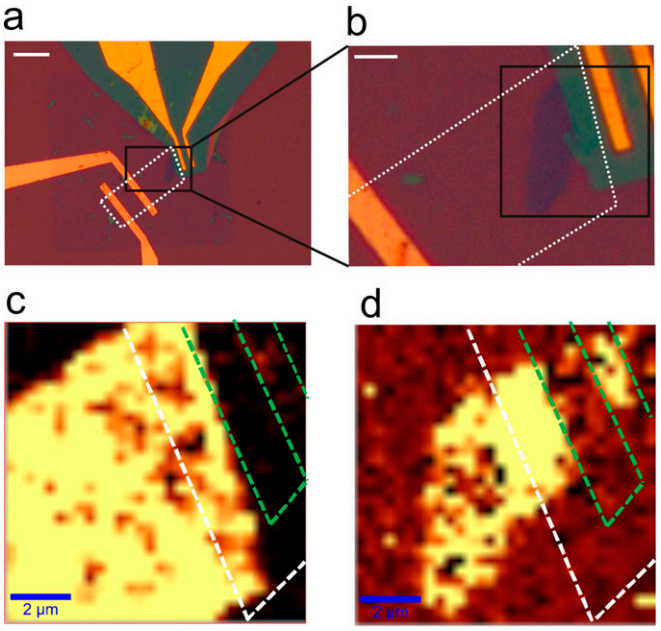

Fig. S7. (*A*) Optical micrograph of a heterojunction device showing a SL-MoS_2 FET top right and s-SWCNT FET bottom left. The white dotted line indicates the extent of the patterned SWCNT film. (Scale bar, 10 μm.) (*B*) Zoom-in of *A* representing the area scanned for spatial photocurrent mapping in Fig. 3*A*. The black outline indicates the scanned area for spatial mapping of the PL and the Raman shift. (Scale bar, 2.5 μm.) (*C*) Spatial map of the Raman shift (3,100–3,250 cm^{-1}), which shows the bright area as the patterned SWCNT film. No Raman signal for the SWCNTs is observed in the MoS_2 contact or channel region marked by green lines. The white boundary indicates the extent of ALD grown alumina. (*D*) PL map of the SL-MoS_2 flake at the A peak (3,700–3,900 cm^{-1}). The region of increased PL intensity represents the shape of the flake as seen in the optical images and the photocurrent map of Fig. 3*A*. No PL signal is observed in the contact regions, indicating PL quenching by the gold. PL from MoS_2 is also observed from the SL-MoS_2 FET channel area, between the contacts.

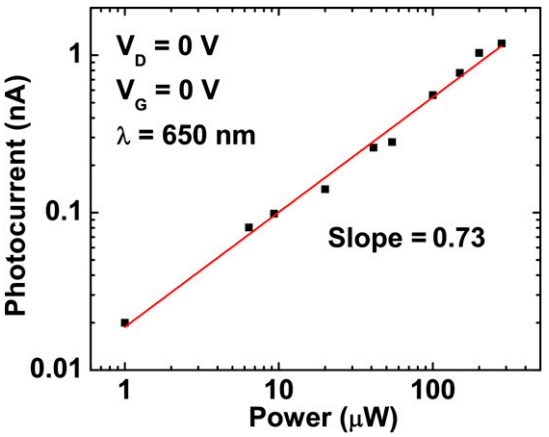

Fig. S8. Power dependence of the photocurrent under zero applied bias. The red line is a linear fit to the data showing a slope of 0.73.